Progress in Natural Science: Materials International 27 (2017) 66–73

Contents lists available at ScienceDirect

Progress in Natural Science: Materials International

journal homepage: www.elsevier.com/locate/pnsmi

Review

Synchrotron radiation X-ray powder diffraction techniques applied in hydrogen storage materials - A review

Honghui Cheng[a,*], Chen Lu[a], Jingjing Liu[a], Yongke Yan[a], Xingbo Han[b,*], Huiming Jin[a], Yu Wang[b], Yi Liu[b], Changle Wu[c]

[a] College of Mechanical Engineering, Yangzhou University, Yangzhou 225127, China
[b] Shanghai Institute of Applied Physics, Chinese Academy of Sciences, Shanghai 201800, China
[c] Test Center, Yangzhou University, Yangzhou 225009, China

ARTICLE INFO

Keywords:
Synchrotron radiation
X-ray powder diffraction
Hydrogen storage materials
Review

ABSTRACT

Synchrotron radiation is an advanced collimated light source with high intensity. It has particular advantages in structural characterization of materials on the atomic or molecular scale. Synchrotron radiation X-ray powder diffraction (SR-XRPD) has been successfully exploited to various areas of hydrogen storage materials. In the paper, we will give a brief introduction on hydrogen storage materials, X-ray powder diffraction (XRPD), and synchrotron radiation light source. The applications of ex situ and in situ time-resolved SR-XRPD in hydrogen storage materials, are reviewed in detail. Future trends and proposals in the applications of the advanced XRPD techniques in hydrogen storage materials are also discussed.

1. Introduction

Hydrogen is very advantageous in the sense that (i) it is a clean burnable fuel, (ii) it possesses a high energy density, and (iii) it is widely distributed all over the globe. In spite of all these advantages, a dependable economic system based on H_2 fuel could not be easily established due to many technical challenges, such as hydrogen production, storage and application. Among these, hydrogen storage presents a huge challenge. It was proposed by U.S. Department of Energy (USDOE) that a hydrogen storage media with 5.5 wt% reversible hydrogen capacity under affordable conditions should be established for commercial onboard applications [1]. Both high compression storage and cryogenic storage modes are considered ineffective due to high cost and safety concerns [2]. Accordingly, the effective means of hydrogen storage system appears to be reversible hydrogen storage materials. A lot of these materials have been investigated but none of them offers the required performances of USDOE. After decades of extensive investigation, it is now concluded that the USDOE aim can be achieved only through light weight materials, particularly with elements having atomic number < 20. In fact, many high capacity materials are known with capacity even more than double the USDOE target. But these hydrides are either too stable or unstable and not reversible under moderate conditions. Hence, research efforts like catalyzing high capacity hydrides, decorating/doping particular sites for tuning the properties, and chemical modifications for enhancing the thermodynamic features and tailoring of new light weight composite systems have been attempted to develop a new material capable of reversibly storing hydrogen under moderate conditions, and meanwhile exhibiting high capacity and quick reaction kinetics.

The properties and performances of materials are strongly correlated to their microstructures. Synchrotron radiation X-ray powder diffraction (SR-XRPD) is a puissant and special characterization technique that exploits the interaction between synchrotron radiation (SR) X-ray and matter to investigate the microstructures of materials. SR-XRPD is more accurate to evaluate phase composition, crystallite size, strain and defect and allows time-resolved studies. Although hydrogen storage materials are a big family consisting of thousands of members, we limit our discussion scope to those materials widely concerned in the present review. We initially address the basic aspects of hydrogen storage materials, X-ray powder diffraction (XRPD), and SR light source. A detailed introduction of recent advances in a variety of SR-XRPD applications in hydrogen storage materials is sequentially indicated. The future trends of the research field are finally discussed.

2. Hydrogen storage materials

The interaction mechanisms between hydrogen and host material can be categorized to physisorptive binding of molecular hydrogen and

Peer review under responsibility of Chinese Materials Research Society.
* Corresponding authors.
E-mail addresses: 31834385@qq.com (H. Cheng), hanxingbo@sinap.ac.cn (X. Han).

http://dx.doi.org/10.1016/j.pnsc.2016.12.007
Received 9 October 2016; Accepted 30 November 2016
Available online 20 January 2017
1002-0071/

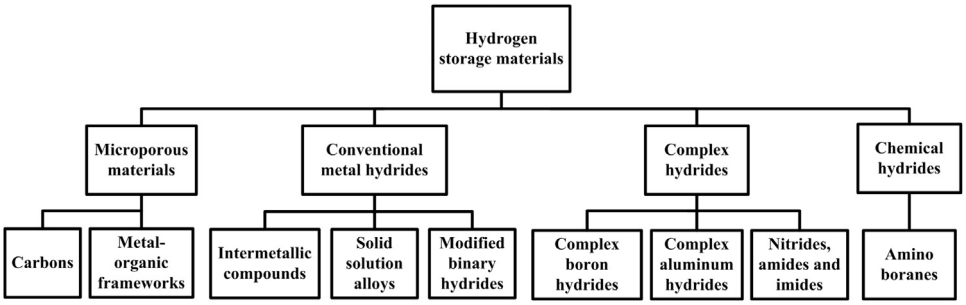

Fig. 1. Family tree of hydrogen storage materials.

chemisorptive binding of atomic hydrogen [3]. The forces involved in physisorption are weak Van der Waals forces. This process usually occurs with fast kinetics because no activation energy barrier is involved. Chemisorption requires energy of >436 kJ mol^{-1} to break the bond of H_2. Therefore, this interaction exhibits slower kinetics. If the barrier is large, the reactants are required to be activated, by either carrying out the reaction at high temperature or introducing catalysts. The catalytic component does not change the basic reaction thermodynamics, but enhance the reaction rate. It is desirable that the employed catalyst is in nano-sized and disperses throughout the system to increase catalyzing efficiency. Hydrogen storage materials are usually classified into four broad categories using a combination of two criteria: (i) the nature of their sorption mechanism, and (ii) the identity of the material itself [4]. As shown in Fig. 1, these four categories are microporous materials, conventional metal hydrides, complex hydrides and chemical hydrides.

Microporous materials have pore dimensions of <2 nm and extraordinarily large surface areas. The amount of adsorbed hydrogen and the surface area are generally in the direct ratio. These materials adsorb H_2 through physisorption. Materials in this category mainly include carbons [5] and metal-organic frameworks (MOFs) [6]. Carbons can be differentiated into a variety of forms such as activated carbons, fullerenes, and carbon nanotubes. MOFs are crystal materials constituted of metal ions or clusters linked by organic bridges. Both carbons and MOFs are striking materials for hydrogen storage, as they have the potential to be reversible and low-cost with facile hydrogen absorption/desorption kinetics and favorable gravimetric capacity. However, the problem is that the materials tend to possess high storage capacities only at low temperatures near the boiling point of liquid N_2. Therefore, one big research challenge for these materials is to increase the hydrogen binding strength to above 15 kJ mol^{-1} H_2.

Conventional metal hydrides store atomic H in the bulk of the materials and have been studied for more than half a century [7,8]. H_2 is split into atomic H on the material surface and then diffuses into its bulk. However, the gravimetric capacity of these materials is mostly too low, or the thermodynamics of H bonding is either too weak or too strong for automotive applications. For example, AlH_3 has fantastic gravimetric capacity (10.07 wt%). Whereas, due to a low formation enthalpy of −6.0–7.6 kJ. mol^{-1} H_2 [9] for AlH_3 directly from Al and H_2, it is unattainable to directly regenerate AlH_3 from H_2 and Al under modest pressure. MgH_2 has a comparatively high gravimetric capacity (7.66 wt%) too, but suffers from too strong binding energy (ΔH=−66–75 kJ. mol^{-1} H_2), demanding about 290 °C to desorb H_2 at 0.1 MPa [10]. Besides, metal hydrides with reasonable cohesive energies, e.g. $LaNi_5H_6$, have good thermodynamics (ΔH=−30–43 kJ. mol^{-1} H_2), but are comprised of heavy transition and rare earth metals, and therefore have low gravimetric densities (1–4 wt%).

Complex hydrides are a kind of ionic compounds which are constituted by metal cations (e.g. often Li^+, Na^+, Mg^{2+}, and Ca^{2+}) and H-containing “complex” anions (e.g. often BH_4^-, AlH_4^-, and NH_{2^-}). Hydrogen atoms and central atoms are covalently bonded in the complex. Thus, complex hydrides are classified as chemisorptive mechanism. Examples of distinguished complex hydrides include $LiBH_4$, $NaAlH_4$ and $LiNH_2$. The strong interest in the hydrides is the result of their uncharacteristically high possible storage capacities (e.g. 18.36 wt% for $LiBH_4$). Nevertheless, there are serious limitations to their practical use, which include high hydrogenation/dehydrogenation temperatures (100–300 °C or even higher), slow kinetics, and high sensitivity to air and moisture. Especially for Li–N–H system, NH_3 liberation during the dehydrogenation reaction is also an issue, because NH_3 is a very strong poison for membranes of polymer electrolyte membrane fuel cell (PEMFC). To this kind of hydrides, the research aim is often to avoid byproducts and lower the hydrogen cohesive energy [11–14].

Chemical hydrides are non-reversible storage materials that require an off-board regeneration process [15]. However, some chemical hydrides have high gravimetric and volumetric capacities, and moderate operating conditions which are often less than 80 °C at 0.1 MPa hydrogen pressure. NH_3BH_3 is a hopeful solid-state chemical hydride with hydrogen content of 19.6 wt%. Hydrogen desorption from NH_3BH_3 is mostly carried out via thermolysis, because it has good storage capacity for automotive applications. The thermolysis of NH_3BH_3 involves three sequential steps occurring at 70–112, 110–200 and 500–1100 °C, with 6.5 wt% H_2 liberated in each step. A primary challenge for NH_3BH_3 is to improve the dehydrogenation rate at low temperatures about 85 °C which is the PEMFC functioning temperature and simultaneously prevent the generation of harmful byproducts (e.g. $(BH)_3(NH)_3$) to electrodes. In addition, avoiding the formation of very stable dehydrogenated products is also a big challenge. [16].

As we know, materials are constructed by atoms. Knowledge of how atoms are arranged into crystalline structures and microstructures is important for understanding of the structure, synthesis and properties of materials. Since hydrides normally exist in powder state, powder diffraction with X-rays or neutrons are the main techniques for finding the atomic arrangements. Because neutrons are sensitive to low atomic number elements, such as hydrogen and boron, and skilled in distinguishing elements with adjacent atomic numbers, such as Fe and Co, isotopes of the same element, or element groups whose atomic numbers are wide apart, such as Pd and H, the extracted information of neutron powder diffraction (NPD) is unique compared to that obtained from XRPD. However, many disadvantages, such as need of large sample, small neutron flux, and low availability, make that NPD is only a supplementary technique to XRPD in the field of hydrogen storage materials.

3. X-ray powder diffraction

X-rays going through a crystal will be scattered by the electron clouds of atoms and bent at different angles. The process is called diffraction. Thanks to its advantages of rapid, non-destructive analysis without troublesome sample preparation, XRPD is extensively used to obtain the structural information of hydrides. In addition, the XRPD instrumentation is flexible, allowing both Bragg-Brentano (flat-plate)

geometry and Debye-Scherrer (capillary) geometry, utilization of pressure cells, furnaces, cryostats, etc., and thus also permitting diverse in situ experiments.

Crystalline material is made of atoms with long-term orderly arrangement in 3D space. The basic repeating unit and the smallest unit that keeps the full symmetry of the crystal structure is unit cell. In some directions (constructive interference), X-ray scattering is strong. While in other directions (destructive interference), the scattering is much weaker. The size and shape of the unit cells determine the directions of constructive interference. The conditions for constructive interference can be described by Bragg's law [17], $2d_{hkl}\sin\theta = n\lambda$, where Miller indices (*hkl*) are used to identify different crystallographic planes, d_{hkl} is the distance between parallel crystallographic planes in the family (*hkl*) and is a geometric function of the size and shape of the unit cell, θ is half of the angle between the incident and scattered beams, n is an integer, and λ is the incident light wavelength, which is typically used in the range 0.5–2.5 Å in crystallographic studies. For a single crystal which has the unit cells with the same orientation and periodicity throughout the bulk, the diffraction corresponding to lattice planes *hkl* will be in unique directions in the 3D space. For materials which exist in the form of polycrystalline consisting of an enormous number of crystals with random orientations, the scattering corresponding to lattice planes *hkl* will give rise to a diffraction ring on area detector. Each ring is made up of a set of closely spaced dots. Each dot represents a diffraction from a single crystallite. The usual representation of a XRPD spectrum is a plot of intensity *v.s.* scattering angle, which can be obtained by integration along the diffraction rings using FIT2D software [18]. The atomic arrangement within unit cells determines the diffraction peaks intensities.

From XRPD data, different information can be acquired, which include (i) qualitative analyses (phase compositions) and quantitative analyses (phase abundances), (ii) Bravais lattice symmetry and lattice parameters, (iii) residual strain (macrostrain), (iv) crystal structure, (v) crystallite size and microstrain, and (vi) evolutions of all aforementioned properties as a function of pressure, time, temperature, gas environment, and so on. To extract abundant structural information from XRPD data, Rietveld refinement software (e.g. often GSAS, FullProf, TOPAS, and RIETAN) are often employed.

4. Synchrotron radiation light source

To laboratory X-ray diffraction (XRD), X-rays are produced by the collision between high energy electrons and a metal target. The radiation is made up of characteristic X-rays corresponding to the target material (Cu, Mo and Cr) and a continuous spectrum. The exploitable X-ray wavelengths corresponding to the $K_{\alpha 1}$ transitions are 1.5404, 0.7093, and 2.2896 Å [19]. To SR-XRD, X-rays are produced by SR facility. In this facility, electrons are produced in electron gun, and thereafter speeded up to near light speed, achieving multi-GeV level energy in booster. The electrons are then injected into an ultra-high vacuum storage ring with several kilometers circumference. In the storage ring, electrons traveling at high speed and forced to change their movement direction under magnetic field, radiate electromagnetic radiation in a narrow cone in their movement direction, called SR. In 1947, SR was firstly observed at General Electric synchrotron in USA. For a long time, it was only considered as a problem since it is the main source of energy loss in high energy particle accelerator. Until the late sixties, SR was found to be valuable for condensed matter research. Since then, an explosive growth in the building of dedicated SR facilities made this a unique tool in many fields. In the 2nd generation synchrotrons, the radiations are produced by bending magnets. In the current 3rd generation ones (Fig. 2), insertion devices (wigglers and undulators) are employed in order to greatly increase the X-ray beam intensity. Now, more than 50 SR facilities have been built in the world. The three most powerful SR facilities are the Super Photon Ring (Spring-8) in Hyogo, Japan, the Advance Photon Source in Argonne (APS), USA, and the European SR Facility (ESRF) in Grenoble, France, with electron energies of 8.0, 7.0 and 6.0 GeV, respectively [20].

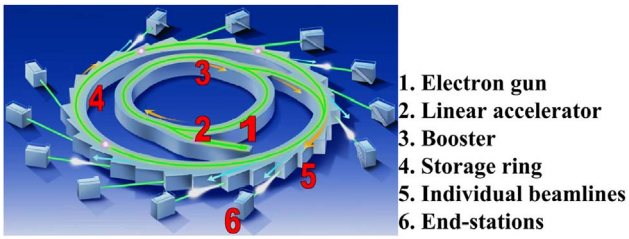

Fig. 2. Illustration of the 3rd generation SR light source.

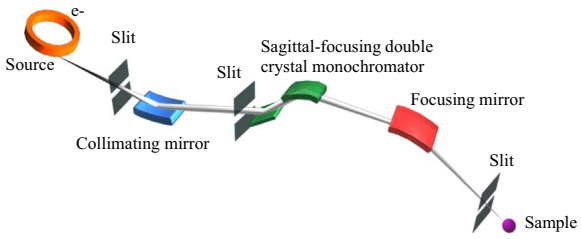

Fig. 3. Schematic illustration of typical optics of SR-XRD beamline.

To SR, beamline refers to the instrumentation that carries SR beam to experimental end-station. It incorporates monochromator, slit, mirror and other devices to select appropriate wavelengths and focus [21]. Schematic illustration of typical optics of SR-XRD beamline is shown in Fig. 3. In the beamline, collimating mirror, monochromator, and focusing mirror are the key optical components. The collimating mirror is used to collimate the beam in vertical direction into parallel light, improving the energy resolution [22]. The monochromator is mostly Si(111) double crystal monochromator, which is employed to create tunable monochromatic X-ray and focus the beam in horizontal direction [21]. The focusing mirror is used to further focalize the beam in vertical direction to the sample point. Experiments employing SR X-ray are conducted in end-station, which is housed inside radiation shielding enclosures (hutches) to guard operators from harmful X-ray. Because operators can not enter the hutches during experiment, the equipments are mostly controlled remotely by computer.

SR has a few of particular properties: (i) high brightness: the brilliance of the X-rays from the 3rd generation sources is 10^5~10^{12} more intense than that from the laboratory sources, which means the time required to record diffraction pattern is significantly reduced and the resolution is much higher; (ii) highly collimated: synchrotron light is parallel, and therefore spreads minimally as it propagates; (iii) wide energy spectrum: this radiation includes a wide range of energies from infrared to hard X-ray, allowing an optimal wavelength selection to reduce absorption either in sample holders and sample or varying wavelengths in experiment; (iv) short pulsed time structure: the ps-level pulse length allows the process resolution on the same time scale. SR provides greater penetration depths than the laboratory equivalent and significantly improves possibilities for both time-resolved and high-resolution in situ experiments.

5. Applications of SR-XRPD

Because of the monochromatic high flux and highly collimated beams, SR-XRPD possesses the main advantages of no $K\alpha_2$ diffraction peaks, high signal/noise ratio, and high angular resolution, which allow the analysis of complex structural details and the observation of complicated peak broadening effects. The extremely high signal/noise ratio of the diffraction pattern makes the data especially good for Rietveld refinement. When combining SR-XRPD with the newest ultra-fast and efficient solid-state detectors, < 0.05 wt% detection level is procurable even when only micrograms of powder are available.

Capillary geometry is the most commonly applied geometry in SR-XRPD, because it has many advantages: (i) it is straightforward to carry out and align; (ii) the resolution is controlled by the diameter of the capillary, smaller diameter means higher resolution; (iii) the sample environment can be controlled and conditioned efficiently. Most experiments in need of fast measurements (phase transformation, reaction kinetics, etc.) generally adopt capillary geometry with fast detectors [23]. SR-XRPD studies can improve our understanding of the correlation between crystal structure, microstructure and hydrogenation ability and allow development of hydrogen storage materials with optimized properties.

5.1. Applications of ex situ SR-XRPD

Use of ex situ SR-XRPD is common in achieving extraordinarily high quality static structural data of hydrogen storage material. Before the experiment, the sample should be finely and uniformly ground to particle sizes less than 20 μm and then loaded into a 0.1–0.5 mm glass capillary and sealed with vacuum grease or epoxy adhesive in argon/nitrogen-filled glove box. The detailed capillary sample preparation method can be referred to the Australian Synchrotron website [24]. In the diffraction process, the sample is kept rotating (1–2 Hz) to eliminate any preferred orientation effects.

Professor Chen's group is prominent in the study of chemical and complex hydrides, especially amide-hydride composite materials and amidoborane system. Recently, they used SR-XRPD data collected with 1.2398 Å X-ray and ambient temperature at station BL14B1, SSRF (Shanghai, China) to uncover the crystal structures by overlapped diffraction peaks deconvolution, determining the intensity of each diffraction peak, pattern index, crystal lattice, space group, lattice constant, and related structure amplitude, etc. [25–29].

Professor Ju's group is good at employing synchrotron techniques to characterize many hydrogen storage materials. They once adopted SR-XRPD with flat-plate geometry to investigate $NaAlH_4$ samples doped with Ce additives and Ti–Zr additives at various hydrogenation stages. The diffraction patterns were measured in the range 2θ=10–80° with a step of $\Delta(2\theta)$=0.02° and 1.38 Å X-ray at station 4B9A, BSRF (Beijing, China). The phase contents and unit cell dimensions of the samples were determined by Rietveld refinements. The results showed that: (i) no Ce crystal was formed during ball-milling, hydrogenation and dehydrogenation, but certain Ce–Al alloys were generated; (ii) lattice constants of $NaAlH_4$ doped with Ce additives were changed, in particular, the *c*-value increased due to the catalyst intercalating into the unit cell; (iii) the lattice constants of $NaAlH_4$ doped with Ti–Zr additives demonstrated no marked difference from the pure samples [30,31].

Brinks et al. collected the diffraction patterns of $NaAlH_4$, Na_3AlH_6 and NaH samples with Ti additives at station BM01B, ESRF. The patterns were collected with steps of $\Delta(2\theta)$=0.003–0.007°. According to the refinement, after ball milling, there are no signs of any Ti-containing phases, which means Ti was in an amorphous state. However, it seemed that a fcc solid solution $Al_{1-x}Ti_x$ appeared in the samples after cycling. Furthermore, TiF_3 added by ball milling resulted in different phases compared to $TiCl_3$/$TiCl_4$. The chlorides produced NaCl, while no NaF was formed by the fluoride [32].

Noritake et al. carried out Li_2NH diffraction experiment at station BL02B2, SPring-8. The diffraction pattern were collected with 0.80 Å X-ray and a 0.01° step from 5° to 75° in 2θ. The charge density distribution in Li_2NH crystal was acquired by the combination of Rietveld method and maximum entropy method (MEM) using ENIGMA program. The results disclosed the crystal structure and lattice constant of Li_2NH, the hydrogen atomic occupation, the charge density distribution of NH^{2-}, and the number of electrons within the spherical region around Li and NH [33,34].

Bowman et al. studied the crystal lattice properties of $LaNi_{5-x}Sn_x$ alloys before and after hydrogenation using high-resolution SR-XRPD at NSLS in the Brookhaven National Laboratory, USA. According to the SR-XRPD data, they detected a range of different responses of the lattice parameters upon cycling. These results indicate that a far more complicated microstructure evolves in company with the changes in P–C–T isotherms at high temperatures [35].

Černý et al. studied anisotropic peak broadening in hydrogen-cycled $LaNi_5$ and substitutional derivatives by SR-XRPD technique. The diffraction patterns were analysed by full pattern fitting (Fullprof) with strain broadening related to local variations of the lattice parameters, and by an individual peak profile fitting (Shadow) based on a dislocation model. Two types of diffraction peak broadening effects were found as a function of the substitution in $LaNi_5$: (i) a decrease of the broadening related to the decrease of the total dislocation density and (ii) a change in the broadening anisotropy related to the change of the nature of the dislocation system involved [36].

Moreover, SR-XRPD were also applied in the study of Pd_5As [37], (La, Mm)$Ni_{5-x}Sn_x$ [38], $LaNi_5Sn$ [39], MgH_2 [40], and $LaNi_{3.55}Mn_{0.4}Al_{0.3}Co_{0.75}$ [41], etc. According to the published literatures in recent years, high-resolution ex situ SR-XRPD is mainly employed to determine phase composition, lattice parameters, crystal structure, crystallite size and microstrain, dislocation density and charge density of hydrogen storage material.

5.2. Applications of in situ SR-XRPD

In situ SR-XRPD is more widely employed compared to ex situ SR-XRPD. To hydrogen storage material, recording of SR-XRPD data throughout the whole chemical reaction allows for reliable conclusions on the reaction mechanism and even thermodynamic properties, especially in combination with quantitative analysis.

For in situ SR-XRPD study of hydrogen storage material, special sample cell, which allows for high X-ray transmission, is vitally important. At the same time, it must have sufficient stability and strength at high temperature and high pressure environment. Two kinds of specialized sample cells are mainly adopted. One is based on capillary with one closed end [42–48]. The other is based on open-ended capillary [48–56]. The adopted capillary materials include special glass, borosilicate glass, quartz (SiO_2) glass, and single crystalline sapphire (Al_2O_3) glass. Glass capillaries give a relatively high amorphous background in the diffraction patters and lower maximum operating temperature, and may react with some high active hydrides at elevated temperatures. Al_2O_3 is characterized by excellent hardness (9 Mohs hardness), high melting point (2053 °C), high tensile strength (275 MPa, RT), low X-ray absorption, and chemically inert to molten hydrides. In addition, the diffraction spots from single crystalline Al_2O_3 capillary can be minimized by rotating the cell and be easily masked out during data integration, or screened by placing lead in front of the diffraction detector. The sample cells (Fig. 4) based on capillary with one closed end are more affordable and more operational. In Fig. 4(a) and (b), the sample cells are mainly assembled from Swagelok or VCR Tee union. One end of the Tee union is linked to the gas system, another is closed, and the other is used for mounting capillary tube with Vespel/graphite ferrule or Loctite/epoxy glue. The reaction temperature is controlled by external calibrated gas blower. Elimination of preferred orientation effects in the collected diffraction data by averaging over the different orientations of the crystallites is completed by oscillating the setup around the capillary axis. Mostly, powder sample is put into an open-ended capillary with smaller diameter, which is then placed inside the in situ sample cell, to prevent breakage of the sample cell capillary from the stress produced by hydrogenation-induced expansion. In Fig. 4(c), the sample cell is especially designed for $LaNi_5$ hydrogenation at room temperature, and is shut by an X-ray-transparent Be cap and sealed with an O-ring. The powder averaging during experiment was realized by using an internal spinner in the reaction cell. This sample cell is not recommended because it includes poisonous metal (Be) and suffers from

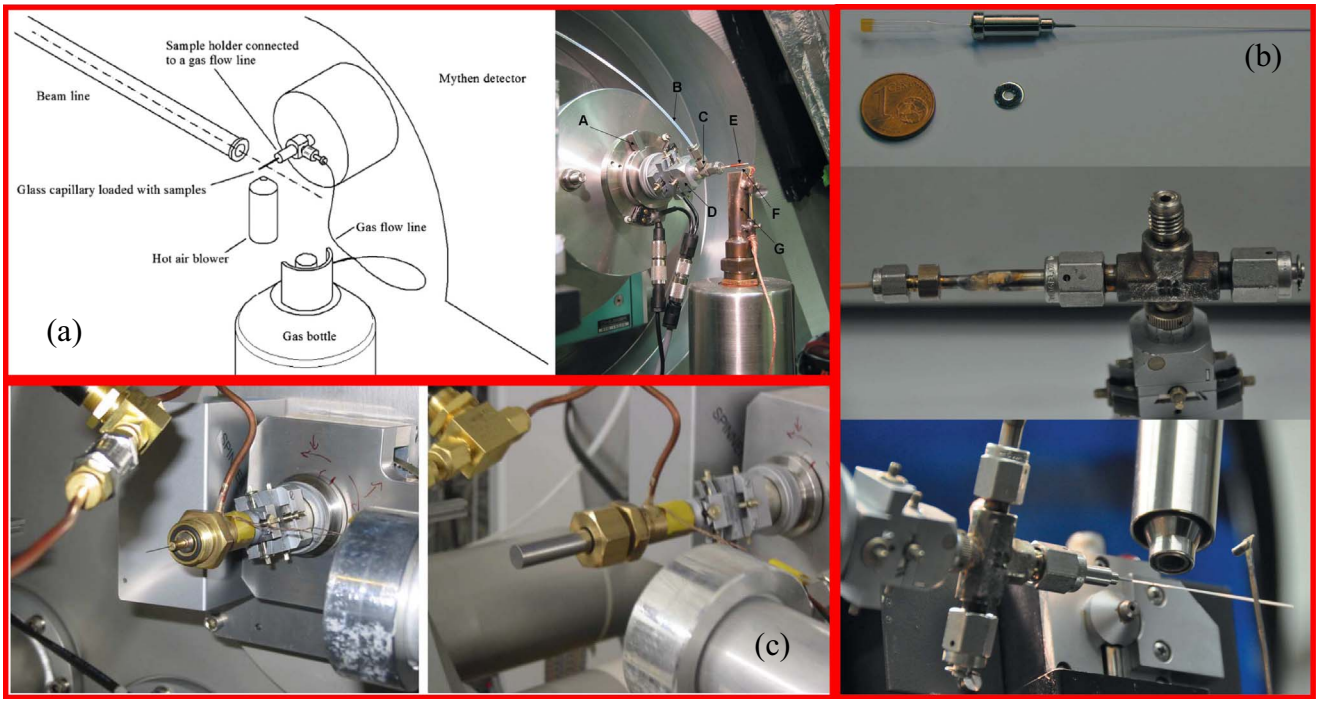

(A) Oscillation device for the sample stage, (B) Gas flow line, (C) Swagelok sample stage, (D) Goniometer head, (E) Capillary reaction cell, (F) Thermocouple, and (G) Hot air blower.

Fig. 4. In situ SR-XRPD sample cells based on capillary with one closed end [42–45,48].

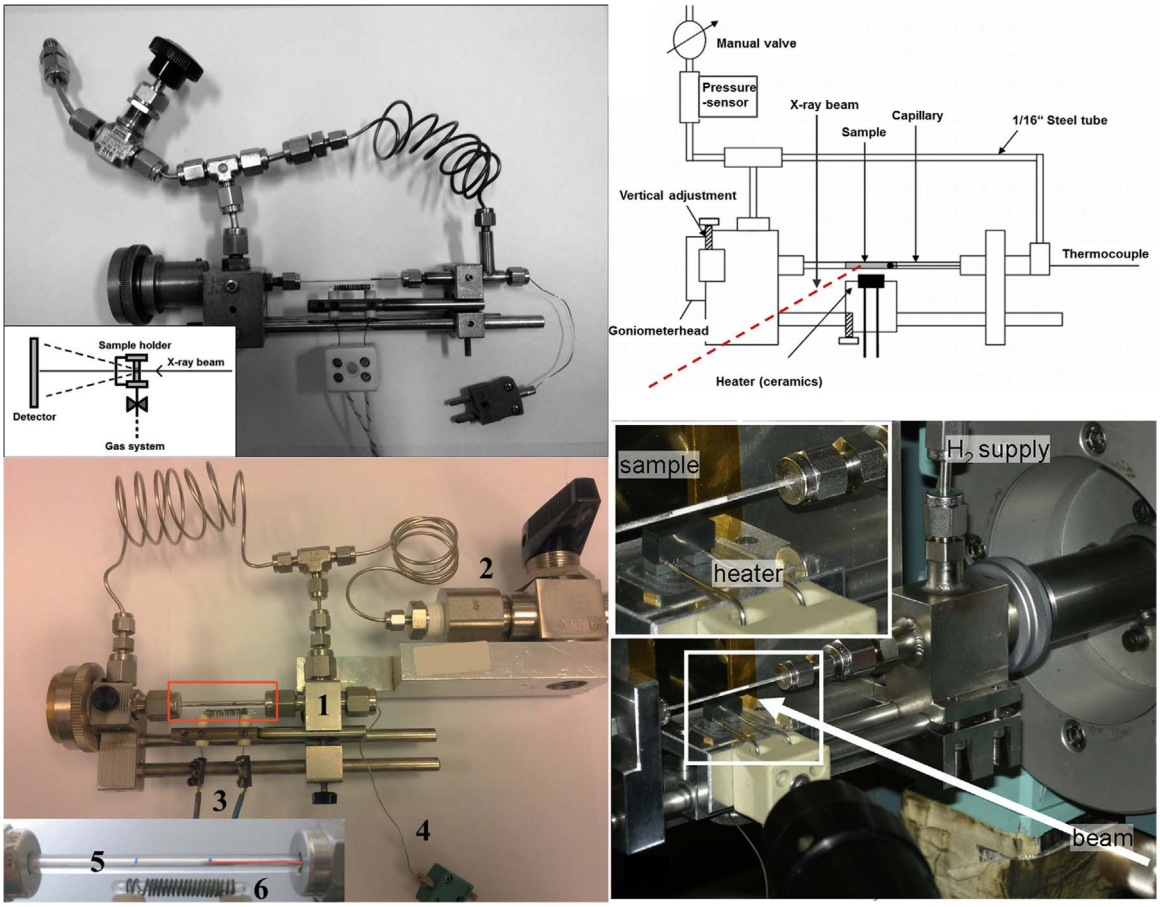

Fig. 5. In situ SR-XRPD sample cells based on open-ended capillary [48–50]. 1. Slider, 2. Valve, 3. Connection for filament heater, 4. Thermocouple, 5. Capillary tube, 6. Filament heater.

temperature rise during hydrogenation [57], and can not run at high pressure and temperature. Jensen and Bösenberg et al [48–50] have developed a series of state-of-the-art in situ sample cells (Fig. 5) based on open-ended capillary. The capillary is fixed and sealed using 1/16′ Swagelok tube fitting and Vespel/graphite. The temperature is measured by thermocouple placed next to the powder sample, and is controlled by blower or resistive heating element. Gas pressure can be equally imposed to both ends of the sample. This can avoid sample displacement during drastic pressure changes. The great advantage of the sample cell is that the sample can be packed in a glove box and kept under an inert atmosphere entirely.

For in situ SR-XRPD, area detector (image plate or CCD) takes precedence over other kinds of detectors, because it gives many merits. Firstly, integration of the intensity from the complete XRD cone can lessen or get rid of preferred orientation effects. Secondly, when chemical reactions occur in the sample cell, the particle size of the product may be markedly bigger than that of the reactants, producing more single-crystal like (spotty) data, instead of the smooth diffraction rings produced by the fine-powder reactants. Thus, area detectors contribute to the improvement of the powder average. Phase analysis is also simplified when the phases can be discriminated on the basis of their azimuthal distribution. Thirdly, diffraction from sources other than the sample can be visually detected, either as diffraction rings with a centre different from the X-ray beam or as diffraction spots located away from the sample diffraction rings [48].

These sample cells have been used successfully in the research of hydrogen storage materials at different instruments, beamlines and synchrotrons for in situ studies under variant conditions. The undermentioned examples will illustrate the diverse information which can be obtained from in situ SR-XRPD data.

(1) Variable temperature in situ SR-XRPD approach was used to study many Cd-based metal borohydrides obtained by mechanochemical synthesis. The multiple powder patterns at variable temperature can be used to solve structure of multiple compounds in the same sample by a method called “decomposition-aided indexing and structure solution”. All observed intensities in the collected diffraction patterns were interpreted for eleven known compounds and four new Cd-based borohydrides. Furthermore, a reliable estimate of the dynamic changes of sample composition and lattice parameters as a function of temperature can be provided by sequential Rietveld refinement of the diffraction data. Thus, it is an effective tool to analyze complicated temperature-induced reaction pathways [58,59].

(2) The hydrogen absorption of $LaNi_5$ alloy has been studied by in situ SR-XPRD and Rietveld refinement. Thanks to the quick diffraction pattern acquisition, the non-equilibrium transient γ ($LaNi_5H_{\sim 3}$) phase, which had never been reported at ambient temperature without prior high temperature cycling, was found to coexists with both α ($LaNi_5H_{0-\sim 0.5}$) and β ($LaNi_5H_{\sim 6}$) phases at nanoscale during the α–β phase transformation. The γ phase partially accommodated the big change of unit cell volume between the α and β phases with varying lattice parameters. Other findings are the variations of the line broadening extent and changes in the line shape during hydrogenation and dehydrogenation. The profile analysis yielded information on the dislocation density and on the dislocation distribution. It was found that the dislocation defects survived the phase transition and were thus hereditable [42,60,61].

(3) $La_{0.5}Ce_{0.5}Ni_4Co$ alloy was studied as a hydrogen compression material using in situ SR-XPRD performed between 263 and 353 K. The SR-XPRD revealed that (i) the relative abundance of the γ-hydride was bigger during the dehydrogenation compared to that during the hydrogenation; its relative amount reached 50 wt% in maximum; (ii) anisotropic strains in all constituent phases during both hydrogenation and dehydrogenation were not evolved; (iii) the formation pressure of the γ-hydride was found to be intensely temperature dependent. Under isobaric conditions, the γ-hydride was produced in larger quantities during dehydrogenation compared to hydrogenation. The phase existed in a slightly narrow temperature interval of 20–30 K [62].

(4) The decomposition processes of α-AlH_3 and γ-AlH_3 were investigated by in situ SR-XPRD and thermal desorption spectroscopy (TDS). The results indicated that a significant anisotropic volume expansion of α-AlH_3 during its heating was observed with the main expansion proceeding along the *a*-axis. The *a*-axis expansion proceeds considerably faster during the fast in situ formation of the α-phase in the γ-AlH_3 decomposition. In the α-AlH_3 decomposition experiment, it seemed that formation of an amorphous phase preceded Al formation and subsequently that the nucleation step limited the Al formation rate. Two parallel decomposition paths of γ-AlH_3 to Al (γ→Al and γ→α→Al) were found. Direct decomposition process (γ→Al) was identified as a predominant one. Nucleation is the rate-limiting step in the Al growth during AlH_3 decomposition process [63].

(5) By means of time-resolved in situ SR-XRPD, the interaction between $LiBH_4$ and different additives (SiO_2, $TiCl_3$, LiCl, and Au) is investigated. It was found that SiO_2 reacted with molten $LiBH_4$ and formed Li_2SiO_3 or Li_4SiO_4 at relatively small amounts of SiO_2, whereas, for higher amounts of SiO_2, only the Li_2SiO_3 phase was observed. A solid-state reaction occurred between $LiBH_4$ and $TiCl_3$ to form LiCl at room temperature. At high temperatures, more LiCl was formed simultaneously with a decrease in the $TiCl_3$ diffracted intensity. LiCl shows some solubility in solid $LiBH_4$ at $t > 100$ °C. Gold is found to react with molten $LiBH_4$ forming a Li-Au alloy with $CuAu_3$-type structure. These studies demonstrate that molten $LiBH_4$ has a high reactivity, and finding a catalyst for this material is a challenge [64].

(6) Ti-rich alloys are regularly applied to hydrogen separation from gas mixtures at medium to high temperatures. Various Ti-based alloys during hydrogenation and dehydrogenation were studied by in situ SR-XRPD performed in H_2 or H_2+10%CO atmosphere to investigate the phase-structural composition and get the crystallographic data of the alloys and their hydrides. Based on the analysis of the in situ diffraction data and the TDS spectrum deconvolution, the dehydrogenation pathways for the γ-$Ti_{0.8}V_{0.05}Cr_{0.15}H_{1.9}$ were brought forward. When hydrogenation of $Ti_{0.8}V_{0.2}$ and $Ti_{0.9}V_{0.1}$ alloys was performed in a mixture of H_2+10%CO, the β-BCC solid solution Ti-V phase was more reactive towards hydrogen absorption and was transformed into the FCC dihydride, while the α-Ti phase was inactive towards hydrogen. Thus, it was concluded that samples which chiefly contain β phase are desirable to be applied to hydrogen separation from gas mixtures containing H_2 and CO. According to this perspective, rapid solidification improves the alloys properties by increasing the quantity of β phase [65,66].

(7) Hydrogen is a very weak scatterer of X-rays compared to metal atoms as the atomic scattering power for X-rays is in proportion to the atomic number. To lightweight hydrides, e. g. $LiBH_4$, the crystal structures including hydrogen atom occupation can be determined unambiguously only by XRD. However, to novel compounds containing light and heavy elements, the structure evaluation is a challenge. Usually, the combined use of several complementary techniques, such as in situ SR-XRPD, NPD, and density functional theory (DFT), is necessary. $LiCe(BH_4)_3Cl$ was synthesized by ball milling of $CeCl_3$–$LiBH_4$ samples in various ratios. In situ SR-XRPD pattern collected at ~160 °C for $CeCl_3$–$LiBH_4$ (1:4), containing the biggest fraction of the novel compound, was used for indexing and structure determination. The diffraction peaks indexing were completed by using the program Dicvol in a body centered cubic cell. The structure was solved in space group $I\bar{4}3m$ by global optimization in direct space

using the program FOX. The crystallographic sites of Ce, B, and Cl were readily localized by SR-XRPD, but the Li and H positions were ambiguous. The combined Rietveld refinement using SR-XRPD and NPD data disclosed three conceivable structure models. However, DFT calculations of the models optimizing the energy of the structures got a structure model for the $LiCe(BH_4)_3Cl$ where Li ions occupy 2/3 of the 12*d* Wyckoff site corresponding to 8 Li ions per unit cell. The study showed that structure model of $LiCe(BH_4)_3Cl$ was derived only by jointly using the three techniques, and would possibly not be acquired with any combination of only two of the methods. [67].

(8) Nanoconfinement is a novel method to enhance the hydrogen storage properties of metal hydrides. Melt-infiltrated $NaAlH_4$ in aerogels with variant pore sizes was studied by in situ SR-XRPD in the temperature between RT and 189 °C at a hydrogen pressure of 160–190 bar. The average apparent crystallite size of nanoconfined $NaAlH_4$ was calculated from SR-XRPD data by Rietveld refinement. The diffraction patterns showed that (i) formation of $NaAlH_4$ nanoparticles only occurred in the nanoporous frameworks with pore sizes between 4 and 100 nm; (ii) bulk $NaAlH_4$ existed from RT to ~170 °C where melting occurred, but partial decomposition and formation of solid Al were detected; (iii) the intimate contact between the aerogel surface and molten $NaAlH_4$ appeared to make it easy for decomposition; (iv) the dehydrogenation mechanism observed from the diffraction patterns of nanoconfined $NaAlH_4$ is in accordance with that of bulk $NaAlH_4$; (v) nanoconfined $NaAlH_4$ might transfer out the porous frameworks during hydrogen release and crystallize as bigger particles on the framwork surface. The study indicated that no chemical reactions between the frameworks and $NaAlH_4$ took place [68].

From the latest literatures [69–78], more and more studies about hydrogen storage materials employed in situ SR-XRPD to explore the natures behind the properties. We can expect that more interesting and stirring in-depth information of these materials will be increasingly disclosed by the novel methods in the near future.

6. Perspectives

Applications of SR-XRPD techniques in hydrogen storage materials have developed enormously since the late nineties. This is partially attributed to enhanced X-ray sources, instrumentation, and more powerful computers, partially because of markedly improved methods, algorithms and structure solution and refinements software. It is expected that all these aspects will be further advanced and strengthened in the next few years. Besides, the high brilliance and collimation of the X-ray source and the great flexibility in experimental design at synchrotron beamlines makes it possible to perform simultaneous measurements, that is to excite and measure diverse signals produced by the sample concurrently. The mapping of the chemical, physical, and crystallographic properties of the sample in 2D and 3D using smart combinations of diffraction, imaging, and spectroscopy is the current evolution of many synchrotron instruments. At present, it is possible to carry out SR-XRPD experiments simultaneously combined with collections of Raman spectroscopy and X-ray absorption fine structure (XAFS) spectroscopy. As an example [79], simultaneous energy-dispersive time-resolved XAFS and XRD were applied to observe the thermal evolution of a MgH_2/Nb_2O_5 mixture [20,23].

Quite recently, the 4th generation light sources, X-ray free electron lasers (XFELs), were commissioned, opening up tremendous new research opportunities. The unique aspects of XFEL radiation are extremely short intense pulses, fields of high amplitude and frequency, and coherence. Thus, XFEL can allow us to carry out unprecedentedly deep researches on ultrafast chemical reactions, ultrafast phase transitions and surface dynamics. Snapshots with atomic resolution and fs time intervals of a molecular dissociation will be made possible. For example, the process of hydrogen molecule separating from host material can be recorded and replayed to be observed in detail [23].

7. Conclusions

One of the significant obstacles for hydrogen utilization is insufficient hydrogen storage capabilities. Therefore, there is an urgent need for developing novel hydrogen storage materials. The deep understanding of crystal structure of hydrogen storage material and the mechanism of hydrogenation/dehydrogenation is very important. SR-XRPD is a versatile and powerful technique, which is extremely important for many aspects of material science. It is an enhancement and optimization over the traditional applications of laboratory XRPD in structure refinement, phase identification, phase quantification, and peak broadening analysis. Additionally, it also allows a lot of experiments that are not accessible using laboratory XRPD, especially in terms of time-resolution, using non-ambient sample environments, and simultaneous experiments. In situ SR-XRPD based on single crystalline Al_2O_3 sample cell with Rietveld refinement is getting an increasingly wide utilization in the research community of hydrogen storage. Simultaneous measurements with SR-XRPD may obtain more and more concern in the near future because these can provide multi-information at the same time. However, we argue that XFEL deserves special attention because it will provide fabulous new research chances.

Acknowledgements

The authors thank all staff members of station BL14B1 (SSRF, China) for the provision of related important information and beneficial discussions. The authors appreciate the financial support from the National Natural Science Foundation of China (No's. 11475145 and 11405252), Yangzhou Foundation for Development of Science and Technology under Grant No. YZ2014041, and the Teaching Reform Project of Yangzhou University under Grant No. YZUJX2014-35B.

References

[1] H. Shao, G. Xin, J. Zheng, X. Li, E. Akiba, Nano Energy 1 (2012) 590–601.
[2] J. Zheng, X. Liu, P. Xu, P. Liu, Y. Zhao, J. Yang, Int. J. Hydrog. Energy 37 (2012) 1048–1057.
[3] D. Pukazhselvan, V. Kumar, S. Singh, Nano Energy 1 (2012) 566–589.
[4] J. Yang, A. Sudik, C. Wolverton, D.J. Siegel, Chem. Soc. Rev. 39 (2010) 656–675.
[5] A. Zuttel, P. Sudan, P. Mauron, T. Kiyobayashi, C. Emmenegger, L. Schlapbach, Int. J. Hydrog. Energy 27 (2002) 203–212.
[6] L.J. Murray, M. Dincă, J.R. Long, Chem. Soc. Rev. 38 (2009) 1294–1314.
[7] G. Sandrock, J. Alloy. Compd. 293–295 (1999) 877–888.
[8] C. Honghui, P. Jinping, C. Wei, C. Demin, Y. Ke, Rare Met. Mat. Eng. 40 (2011) 1921–1925.
[9] L.E. Klebanoff, J.O. Keller, Int. J. Hydrog. Energy 38 (2013) 4533–4576.
[10] J.C. Crivello, R.V. Denys, M. Dornheim, M. Felderhoff, D.M. Grant, J. Huot, T.R. Jensen, P. de Jongh, M. Latroche, G.S. Walker, C.J. Webb, V.A. Yartys, Appl. Phys. A 122 (2016) 1–17.
[11] I. Jain, P. Jain, A. Jain, J. Alloy. Compd. 503 (2010) 303–339.
[12] B.-X. Dong, J. Ge, Y.-L. Teng, J.-J. Gao, L. Song, J. Mater. Chem. A 3 (2015) 905–911.
[13] B.-X. Dong, J.-J. Gao, Y.-L. Teng, H. Tian, L.-Z. Wang, Int. J. Hydrog. Energy 41 (2016) 5371–5377.
[14] B.-X. Dong, L.-T. Chen, Y.-L. Teng, J.-J. Gao, H. Tian, J. Mater. Sci. 51 (2016) 911–916.
[15] C.W. Hamilton, R.T. Baker, A. Staubitz, I. Manners, Chem. Soc. Rev. 38 (2009) 279–293.
[16] R.B. Biniwale, S. Rayalu, S. Devotta, M. Ichikawa, Int. J. Hydrog. Energy 33 (2008) 360–365.
[17] S. Wilkins, Acta Crystallogr. A 69 (2013) 1–4.
[18] A. Hammersley, S. Svensson, M. Hanfland, A. Fitch, D. Hausermann, High. Press. Res. 14 (1996) 235–248.
[19] O.H. Seeck, B. Murphy, X-ray Diffraction: Modern Experimental Techniques, CRC Press, Boca Raton, 2015.
[20] G. Walker, Solid-state Hydrogen Storage Materials and Chemistry, CRC Press, Boca Raton, 2008.
[21] M. Isshiki, Y. Ohishi, S. Goto, K. Takeshita, T. Ishikawa, Nucl. Instrum. Methods Phys. Res. A 467–468 (2001) 663–666.
[22] Y. Tie-Ying, W. Wen, Y. Guang-Zhi, L. Xiao-Long, G. Mei, G. Yue-Liang, L. Li, L. Yi, L. He, Z. Xing-Min, Z. Bin, L. Ting-Kun, Y. Ying-Guo, L. Zhong, Z. Xing-Tai,

G. Xing-Yu, Nucl. Sci. Tech. 26 (2015) 020101-1–020101-5.
[23] S. Mobilio, F. Boscherini, C. Meneghini, Synchrotron Radiation: Basics, Methods and Applications, Springer, Berlin, 2014.
[24] ⟨http://www.asls.org.au/aussyncbeamlines/powder-diffraction/samples/sample-types⟩
[25] C. Wu, G. Wu, Z. Xiong, X. Han, H. Chu, T. He, P. Chen, Chem. Mater. 22 (2010) 3–5.
[26] L. Liu, G. Wu, W. Chen, Z. Xiong, T. He, P. Chen, Int. J. Hydrog. Energy 40 (2015) 429–434.
[27] J. Chen, Y.S. Chua, H. Wu, Z. Xiong, T. He, W. Zhou, X. Ju, M. Yang, G. Wu, P. Chen, Int. J. Hydrog. Energy 40 (2015) 412–419.
[28] T. He, H. Wu, G. Wu, Z. Li, W. Zhou, X. Ju, D. Xie, P. Chen, J. Mater. Chem. A 3 (2015) 10100–10106.
[29] J. Chen, T. He, G. Wu, Z. Xiong, L. Liu, X. Ju, P. Chen, J. Phys. Chem. C 118 (2014) 13451–13459.
[30] C. Wan, X. Ju, Y. Qi, Y. Zhang, S. Wang, X. Liu, L. Jiang, J. Alloy. Compd. 481 (2009) 60–64.
[31] C. Wan, X. Ju, Y. Qi, S. Wang, X. Liu, L. Jiang, J. Alloy. Compd. 486 (2009) 436–441.
[32] H. Brinks, C. Jensen, S. Srinivasan, B. Hauback, D. Blanchard, K. Murphy, J. Alloy. Compd. 376 (2004) 215–221.
[33] T. Noritake, H. Nozaki, M. Aoki, S. Towata, G. Kitahara, Y. Nakamori, S.-I. Orimo, J. Alloy. Compd. 393 (2005) 264–268.
[34] E. Nishibori, M. Takata, K. Kato, M. Sakata, Y. Kubota, S. Aoyagi, Y. Kuroiwa, M. Yamakata, N. Ikeda, J. Phys. Chem. Solids 62 (2001) 2095–2098.
[35] R.C. Bowman Jr., C.A. Lindensmith, S. Luo, T.B. Flanagan, T. Vogt, J. Alloy. Compd. 330–332 (2002) 271–275.
[36] R. Černý, J.M. Joubert, M. Latroche, A. Percheron-Guégan, K. Yvon, J. Appl. Crystallogr. 33 (2000) 997–1005.
[37] H. Kohlmann, M. Vasseur, A. Sayede, G. Lefevre, J.M. Sander, S. Doyle, J. Alloy. Compd. 664 (2016) 256–265.
[38] O.Y. Khyzhun, M.V. Lototsky, A.B. Riabov, C. Rosenkilde, V.A. Yartys, S. Jørgensen, R.V. Denys, J. Alloy. Compd. 356–357 (2003) 773–778.
[39] M. Sato, M. Stange, J.P. Maehlen, V.A. Yartys, J. Alloy. Compd. 397 (2005) 165–168.
[40] T. Noritake, S. Towata, M. Aoki, Y. Seno, Y. Hirose, E. Nishibori, M. Takata, M. Sakata, J. Alloy. Compd. 356 (2003) 84–86.
[41] J.M. Joubert, R. Černý, M. Latroche, A. Percheron-Guégan, K. Yvon, J. Alloy. Compd. 265 (1998) 311–314.
[42] J. Joubert, R. erny, M. Latroche, A. Percheron-Guégan, B. Schmitt, Acta Mater. 54 (2006) 713–719.
[43] N.V.Y. Scarlett, M.R. Rowles, K.S. Wallwork, I.C. Madsen, J. Appl. Crystallogr. 44 (2011) 60–64.
[44] N.V. Scarlett, I.C. Madsen, B.I. Whittington, J. Appl. Crystallogr. 41 (2008) 572–583.
[45] X.Q. Tran, S.D. Nald, Q.F. Gu, K. Nogita, J. Alloy. Compd. 636 (2015) 249–256.
[46] P. Norby, J. Am. Chem. Soc. 119 (1997) 5215–5221.
[47] E.K. Andersen, I.G.K. Andersen, P. Norby, J.C. Hanson, J. Solid State Chem. 141 (1998) 235–240.
[48] T.R. Jensen, T.K. Nielsen, Y. Filinchuk, J.-E. Jorgensen, Y. Cerenius, E. Gray, C.J. Webb, J. Appl. Crystallogr. 43 (2010) 1456–1463.
[49] B.R. Hansen, K.T. Møller, M. Paskevicius, A.-C. Dippel, P. Walter, C.J. Webb, C. Pistidda, N. Bergemann, M. Dornheim, T. Klassen, J.-E. Jørgensen, T.R. Jensen, J. Appl. Crystallogr. 48 (2015) 1234–1241.
[50] U. Bösenberg, C. Pistidda, M. Tolkiehn, N. Busch, I. Saldan, K. Suarez-Alcantara, A. Arendarska, T. Klassen, M. Dornheim, Int. J. Hydrog. Energy 39 (2014) 9899–9903.
[51] P.J. Chupas, K.W. Chapman, C. Kurtz, J.C. Hanson, P.L. Lee, C.P. Grey, J. Appl. Crystallogr. 41 (2008) 822–824.
[52] K.T. Moller, B.R.S. Hansen, A.-C. Dippel, J.-E. Jorgensen, T.R. Jensen, Z. Anorg. Allg. Chem. 640 (2014) 3029–3043.
[53] B.S. Clausen, G. Steffensen, B. Fabius, J. Villadsen, R. Feidenhans'l, H. Topsøe, J. Catal. 132 (1991) 524–535.
[54] P.J. Chupas, M.F. Ciraolo, J.C. Hanson, C.P. Grey, J. Am. Chem. Soc. 123 (2001) 1694–1702.
[55] W.S. Eu, W.H. Cheung, M. Valix, J. Synchrotron Radiat. 16 (2009) 842–848.
[56] H. Karaca, J. Hong, P. Fongarland, P. Roussel, A. Griboval-Constant, M. Lacroix, K. Hortmann, O.V. Safonova, A.Y. Khodakov, Chem. Commun. 46 (2010) 788–790.
[57] E.M. Gray, D.J. Cookson, T.P. Blach, J. Appl. Crystallogr. 39 (2006) 850–855.
[58] D.B. Ravnsbæk, L.H. Sørensen, Y. Filinchuk, F. Besenbacher, T.R. Jensen, Angew. Chem. Int. Ed. 51 (2012) 3582–3586.
[59] D.B. Ravnsbæk, Y. Filinchuk, R. Cerný, T.R. Jensen, Z. Krist. Cryst. Mater. 225 (2010) 557–569.
[60] E.M. Gray, T.P. Blach, M.P. Pitt, D.J. Cookson, J. Alloy. Compd. 509 (2011) 1630–1635.
[61] E. Wu, E. MacA. Gray, D.J. Cookson, J. Alloy. Compd. 330–332 (2002) 229–233.
[62] A.B. Riabov, R.V. Denys, J.P. Maehlen, V.A. Yartys, J. Alloy. Compd. 509 (2011) S844–S848.
[63] J.P. Maehlen, V.A. Yartys, R.V. Denys, M. Fichtner, C. Frommen, B.M. Bulychev, P. Pattison, H. Emerich, Y.E. Filinchuk, D. Chernyshov, J. Alloy. Compd. 446–447 (2007) 280–289.
[64] L. Mosegaard, B. Møller, J.E. Jørgensen, Y. Filinchuk, Y. Cerenius, J.C. Hanson, E. Dimasi, F. Besenbacher, T.R. Jensen, J. Phys. Chem. C 112 (2008) 1299–1303.
[65] S. Suwarno, J.K. Solberg, J.P. Maehlen, B. Krogh, V.A. Yartys, Int. J. Hydrog. Energy 37 (2012) 7624–7628.
[66] S. Suwarno, J.K. Solberg, J.P. Maehlen, B. Krogh, B.T. BØRresen, E. Ochoa-Fernandez, E. Rytter, M. Williams, R. Denys, V.A. Yartys, T. Nonferr, Metal. Soc. 22 (2012) 1831–1838.
[67] M.B. Ley, D.B. Ravnsbæk, Y. Filinchuk, Y.-S. Lee, R. Janot, Y.W. Cho, J. Skibsted, T.R. Jensen, Chem. Mater. 24 (2012) 1654–1663.
[68] T.K. Nielsen, P. Javadian, M. Polanski, F. Besenbacher, J. Bystrzycki, T.R. Jensen, J. Phys. Chem. C 116 (2012) 21046–21051.
[69] S. Hino, H. Grove, T. Ichikawa, Y. Kojima, M.H. Sørby, B.C. Hauback, Int. J. Hydrog. Energy 40 (2015) 16938–16947.
[70] M. Stange, J.P. Maehlen, V.A. Yartys, P. Norby, W. van Beek, H. Emerich, J. Alloy. Compd. 404–406 (2005) 604–608.
[71] J.P. Maehlen, V.A. Yartys, A.B. Riabov, A. Budziak, H. Figiel, J. Zukrowski, J. Alloy. Compd. 38 (2007) 140–145.
[72] R. Denys, A. Riabov, J. Maehlen, M. Lototsky, J. Solberg, V. Yartys, Acta Mater. 57 (2009) 3989–4000.
[73] R.V. Denys, A.A. Poletaev, J.P. Maehlen, J.K. Solberg, B.P. Tarasov, V.A. Yartys, Int. J. Hydrog. Energy 37 (2012) 5710–5722.
[74] A.A. Poletaev, R.V. Denys, J.P. Maehlen, J.K. Solberg, B.P. Tarasov, V.A. Yartys, Int. J. Hydrog. Energy 37 (2012) 3548–3557.
[75] R.V. Denys, V.A. Yartys, C.J. Webb, Inorg. Chem. 51 (2012) 4231–4238.
[76] K.T. Moller, M.B. Ley, P. Schouwink, R. Cerny, T.R. Jensen, Dalton Trans. 45 (2016) 831–840.
[77] K. Užarević, V. Štrukil, C. Mottillo, P.A. Julien, A. Puškarić, T. Friščić, I. Halasz, Crys. Growth Des. 16 (2016) 2342–2347.
[78] T. Friščić, I. Halasz, P.J. Beldon, A.M. Belenguer, F. Adams, S.A.J. Kimber, V. Honkimäki, R.E. Dinnebier, Nat. Chem. 5 (2013) 66–73.
[79] T.K. Nielsen, T.R. Jensen, Int. J. Hydrog. Energy 37 (2012) 13409–13416.